Linking the Intrinsic Electrical Response of Ferroelectric Devices to Material Properties by means of Impedance Spectroscopy

Lorenzo Benatti, Sara Vecchi, Francesco Maria Puglisi
DIEF, Università di Modena e Reggio Emilia, Via P. Vivarelli 10/1, 41125 Modena, Italy
phone: (+39) 059-2056320 email: lorenzo.benatti@unimore.it

***Abstract*— Ferroelectric devices have gained attention in recent years as a potential solution for ultra-low power computing due to their ability to act as memory units and synaptic weights in brain-inspired architectures. One way to study the behavior of these devices under different conditions, particularly the influence of material composition and charge trapping on ferroelectric switching, is through impedance spectroscopy. However, the parasitic impedance of the metal lines that contact the electrodes of the device can affect the measured response and interpretation of the results. In this study, we examined the frequency response of ferroelectric tunnel junctions (FTJs) with a metal-dielectric-ferroelectric-metal (MDFM) stack at various voltages, starting from the analysis of single layer capacitors (MFM and MDM) to better interpret FTJ's results. To accurately assess the intrinsic response of the device, we developed a method that estimates and removes the parasitic access impedance contribution, which was validated by means of physics-based simulations. This method allows quantifying the intrinsic device-level variability of FTJs and, for the first time, to investigate the relation between the thickness of the dielectric layer, the equivalent phase composition of the ferroelectric material, and the magnitude of the peak in the frequency response, often assumed to be related to charge trapping only.**

Keywords – Ferroelectric Tunnel Junction, Capacitance, Small signal model, Neuromorphic.

I. INTRODUCTION

In the last decade the technological research on computer sciences and electronics promoted enormous improvements in terms of computational capability, data analysis and development of autonomous systems, with notable consequences in the advancements of Artificial Intelligence [1], Internet of Things (IoT) [2] and Big Data management [3]. However, these improvements are ever-increasingly revealing the limitations of typical CMOS computing architectures, e.g., scaling, thermal and energy efficiency constraints [4]–[6]. In particular, the latter is mainly due to the intrinsic separation of the processing and memory units (known as Von Neumann bottleneck (VNB)) and their constant need to communicate [7], [8]. Consequently, a change of paradigm is urgently needed in order to comply with the modern technological requirements in a responsible and sustainable way [9].

Research is currently actively investigating innovative circuit designs [10]–[12] and emerging memory concepts [13]–[15] to overcome the CMOS limitations and comply with the high density and fast data storage needs, building the foundations for logic in memory [16]–[18] and brain-inspired computing [19]–[21], both merging calculus and storage within the same circuital elements.

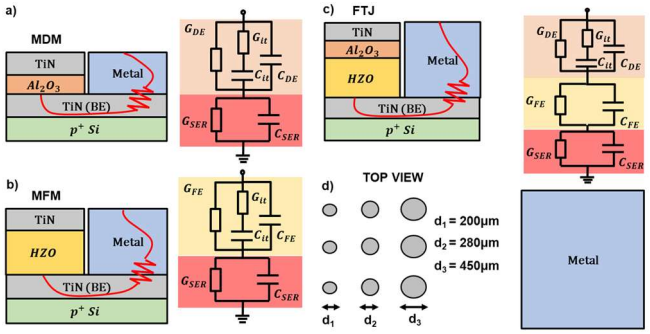

Fig. 1 – Sectional schematic and small-signal model of our (a) MDM, (b) MFM, and (c) FTJ. For each device, the BE is shared and can be reached by a common metal pad. d) Top view (common to all samples), showing the access metal pad and devices with different area.

Among the explored solutions, some of the most promising candidates to lead this technological transition can be found in ferroelectric hafnium zirconium oxide (HZO) based devices [22]–[24] combining remarkable advantages, such as low power consumption, CMOS compatibility, fast access speeds, high-scalability, low footprint, and non-volatility. In particular, the devices studied in this work are ferroelectric tunnel junction (FTJ) memories consisting of a metal-dielectric (DE)-ferroelectric (FE)-metal (MDFM) stack which act as synaptic elements in neuromorphic circuits [25]–[27] with a non-destructive read-out [28], [29]. The information is stored by means of the device remnant polarization, that can be read by sensing the leakage current upon the application of a small voltage pulse. Also, the characteristics of these devices allow for specific tailoring of the operational conditions (e.g., speed and voltage) to best suit different specific applications (e.g., microwave applications or synaptic weights in neural networks)[30], [31], highlighting the flexibility of this technological solution. However, a detailed and comprehensive electrical characterization for different conditions is needed before a dependable introduction of FTJs in actual circuits.

Impedance spectroscopy [32] is a common technique used to investigate the role of each layer (FE and DE) and charge trapping in ferroelectric switching. To estimate the trapped charge response, the G_p/ω peak is often used as a parameter, where G_p is the equivalent conductance in the total admittance of the device under test ($Y(\omega) = j\omega C_p//G_p$). This value is obtained through capacitance-frequency/conductance-frequency (C-f/G-f) measurements, in which a small-signal with a varying frequency is applied on top of a bias voltage. This technique allows for a detailed analysis of the electrical response of ferroelectric devices. However, especially when investigating lab-level samples, test devices may be strongly

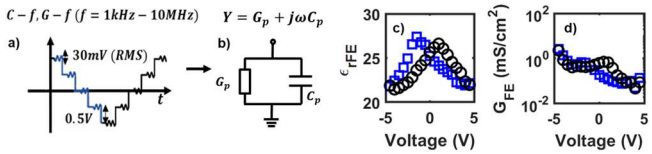

Fig. 2 – a) Multi-voltage C-f/G-f measure starting from positive voltages (blue) and negative voltages (black). For each bias, a small ac signal (30mV) with frequencies from 1kHz to 10MHz is superimposed. b) The total measured admittance ($Y(\omega) = j\omega C_p//G_p$) is analysed with the models of Fig. 1a-b-c. c-d) Example of $\epsilon_{r\,FE}(V)$ and $G_{FE}(V)$ extracted by the model for different polarizations [36], respecting the same colour code as in a).

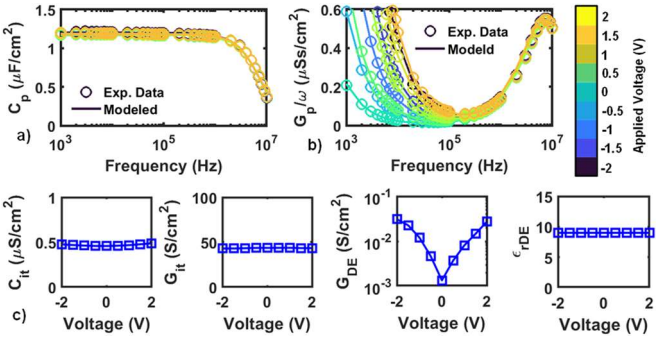

Fig. 3 – a-b) Experimental C_p and G_p/ω values (symbols) and model predictions (lines) at different voltages for an MDM capacitor with t_{DE} = 6nm and diameter d = 280μm. c) Voltage dependence of the extracted model parameters, i.e., the small-signal trap response (C_{it} and G_{it}), G_{DE}, and ϵ_{rDE}.

affected by the parasitic impedance of the metal lines (or broken access device [33], [34]) contacting the electrodes of the device, which is not always negligible and may strongly alter the measured response, with consequences on the interpretation of the results.

In this research, we extend our conference paper [35] and expand upon our previous findings on the validation of the small-signal model for ferroelectric tunnel junctions (FTJs) [33], [34], also used to investigate aging mechanisms [36], and examine the electrical response of FTJs with a metal-dielectric-ferroelectric-metal (MDFM) stack at various voltages through multi-voltage capacitance-frequency/conductance-frequency (C-f/G-f) measurements.

We compare the results of these measurements to those obtained from single layer capacitors (MFM and MDM) to gain a deeper understanding of the electrical properties of these devices. To accurately model the electrical response of the FTJs, we employed small signal models (shown in Fig. 1 a-b-c) that consider: *i*) the distinct leakage and capacitance paths for each layer, *ii*) the first order defects contribution, and *iii*) an equivalent parasitic impedance (Z_{SER}) in series with the device, which is modeled as the parallel of C_{SER} and G_{SER}. The extracted Z_{SER} parameters were validated through physics-based simulation with the Ginestra® [37] simulation platform and then subtracted from the measured response to reveal the intrinsic response and device-level variability. The extracted intrinsic response is then compared with simulations of the intrinsic device to further confirm the dependability of the proposed approach and better interpret the results.

The paper is organized as follows: Section II presents the details of the performed experiments and the studied devices, together with their small-signal model. In Section III we analyze the outcomes obtained by the single-layer capacitors (MDM and MFM) characterization, the validation of the extracted Z_{SER}, and the intrinsic device-to-device variability. In Section IV we repeat the same study on FTJs. In Section V

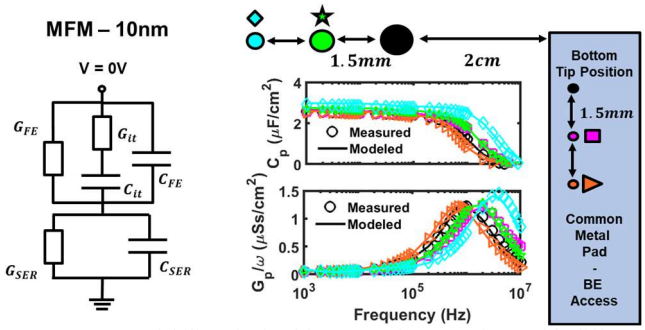

Fig. 4 – MFM variability obtained by measuring capacitors with different areas and different bottom probe positions (expressed with different symbols in the top view). Experimental data (symbols) at 0V are reproduced by the small-signal model (lines). Devices with different areas (cyan, green, black) are measured with the same bottom tip position (black), while the device with the largest area (black) is measured with three different bottom tip positions (black, magenta, orange).

we then compare and discuss the relation found by varying the dielectric and ferroelectric thicknesses (t_{DE} and t_{FE}) in intrinsic FTJ devices and compare the results versus simulations. Conclusions follow.

II. Device and Experiments

We study MFM, MDM, and FTJ frequency response by performing multi-voltage C-f/G-f measurements, as shown in Fig. 2a-b. The FTJs consist of a TiN/Al_2O_3 (DE)/HZO (FE)/TiN stack, with 10nm HZO and different dielectric thicknesses (2-2.5-3-3.5nm). MFM capacitors have t_{FE} = 10nm while MDM have t_{DE} = 6-8-10nm. For each sample, we measured devices with diameter d = 200-280-450 μm. Details of the fabrication process are reported in [28]. The cross-sectional schematics, together with the relative small-signal model and the samples top view are shown in Fig. 1. All devices, provided by NaMLab, consist in capacitors with a shared bottom TiN electrode (BE) that can be contacted via a metal pad. C-f/G-f measurements are executed by applying a stair-case voltage ramp (MFM: [-3 +3] V, MDM: [0 +1] V, FTJ: [-4 +4] V, step 0.5 V), superposing, for each bias, a 30mV RMS AC signal with frequency sweeping from 1kHz to 10MHz. MFM and FTJs are measured for both negative and positive voltages to check the expected relation between the model parameters (specifically the FE permittivity (ϵ_{rFE}) and conductance (G_{FE}) as depicted in Fig. 2c-d) and the applied voltage polarity as well as the ferroelectric polarization. We also limited the bias to a safe range, in order to prevent device degradation and, ultimately, device breakdown. MDM capacitors have been measured only in a small range ([0 +1] V) since, for simplicity, the analysis and comparison with other devices will be focused only on the results obtained at 0V DC bias. However, the MDM model is able to reproduce C_p and G_p/ω profiles (Fig. 3a-b) for higher bias ranges and accounts for the conductance (G_{DE}) voltage dependance, as reported in Fig. 3c for an MDM with t_{DE} = 6nm. Furthermore, the small signal trap response is found to be weakly influenced by applied bias, which makes investigating large voltage ranges superfluous. Fig. 1a-b-c shows, for each device, the compact small-signal model used to map the total measured admittance (the parallel of an overall measured capacitance, C_p, and conductance, G_p) to specific layer-related parameters, Fig. 2b. The models account for a capacitance and conductance path for each layer (to separately consider the leakage of each layer), and a series impedance Z_{SER}

This article has been accepted for publication in IEEE Transactions on Device and Materials Reliability. This is the author's version which has not been fully edited and content may change prior to final publication. Citation information: DOI 10.1109/TDMR.2023.3261441

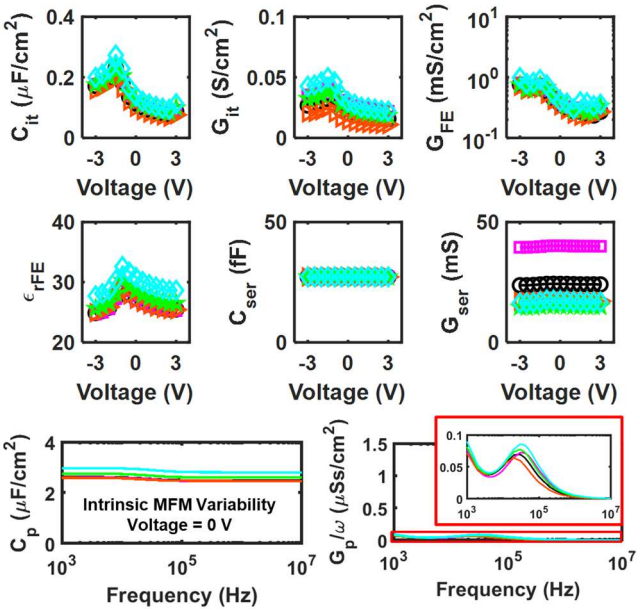

Fig. 5 – Extracted MFM model parameters and intrinsic response of devices in Fig. 4 (same symbols and colours), the latter obtained by removing the series impedance component (C_{SER} and G_{SER}) from the MFM model.

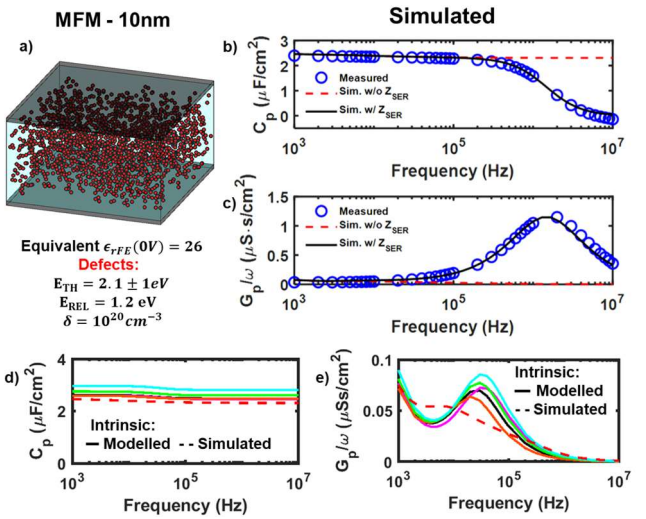

Fig. 6 – a) Simulated MFM stack. From model extraction we imposed an equivalent $\epsilon_{rFE}(0V) = 26$, and we included oxygen vacancy defects in the HfO_2 bulk having thermal E_{TH} = 2.1±1 eV and relaxation E_{REL} = 1.2 eV energies [44] (defects density $\delta = 10^{20} cm^{-3}$, normal distribution centered at 5nm). b-c) Validation of Z_{SER}. Simulations of the MFM structure in a) with a series impedance with a value corresponding to the extracted Z_{SER} allows reproducing the measured C_p and G_p/ω profiles. d-e) Comparison between simulated (dashed lines) and extracted (solid lines) intrinsic C_p and G_p/ω profiles.

(C_{SER}//G_{SER}) to model the parasitic impedance of the access metal lines, which cannot be removed with open-circuit and/or short-circuit compensation [33], [34], which are however performed before the measurements. A C_{it}-G_{it} branch is also inserted between the TiN electrodes (for MFM and MDM) to model to the first order the presence of interface defects at the parasitic TiON / TiAlO layers caused by post-deposition annealing [28], [38]. To simplify the overall FTJ model, we included only a single C_{it}-G_{it} branch across DE to consider the equivalent effect of all interface's defects (M-DE, DE-FE, FE-M), as they are most likely mainly located at the DE-FE interface [39], [40]. Different other attempts in positioning this branch have been tried, without meaningful and relevant

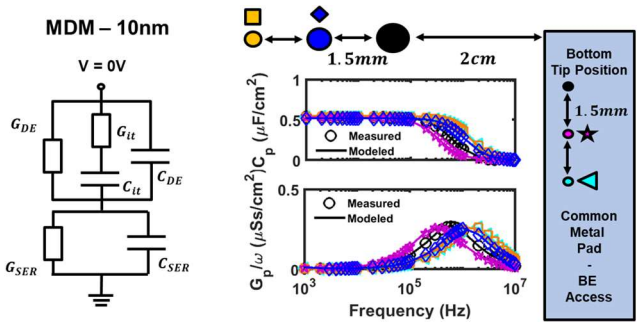

Fig. 7 – MDM with t_{DE} = 10nm measured device-to-device variability obtained by measuring capacitors with different areas and different bottom probe positions (expressed with different symbols in the top view). Experimental data (symbols) at 0V are reproduced by the small-signal model (lines). Devices with different areas (black, blue, yellow) are measured with the same bottom tip position (black), while the device with the larger area (black) is measured with three different bottom tip positions (black, magenta, cyan).

results [34]. Though the model can, with no a priori constraints, reproduce the expected voltage dependence of all parameters for different polarizations (e.g., the typical butterfly-shaped ferroelectric permittivity, ϵ_{rFE}, vs. voltage relation [38], Fig. 2b), the MFM and FTJ results are hereafter reported, for simplicity, only for positive polarization (i.e., +3(+4) V → -3(-4) V). Notice that ϵ_{rFE} represents an effective permittivity, accounting for both orthorhombic (i.e., ferroelectric) and non-ferroelectric phases present in the FE [33], [34], [41].

III. Single Layer Capacitors

In order to better understand the response of materials and defects, we began by studying MFM and MDM single layer capacitors. Fig. 4 illustrates the small-signal model for MFM capacitors and the measurement results for various MFM devices at 0V in terms of C_p and G_p/ω, along with modeled profiles. To investigate the effect of access impedance, we measured the same device with the tip positioned at different locations on the metal pad (resulting in different current paths to the capacitor) as well as devices with different areas but with the tip position fixed on the metal pad. This allowed us to examine the electrical response of these devices and how it is influenced by various factors.

Fig. 5 reports the comparison of the extracted parameters for each voltage and for each device (different symbols and colors), emphasizing a strong device-level variability especially in the series conductance (G_{SER}). Removing Z_{SER} from the model and keeping the other parameters fixed, it is possible to retrieve the intrinsic MFM C_p and G_p/ω profiles (Fig. 5). Results show that: *i*) the intrinsic device-level dispersion is much smaller than what observed in Fig. 4; *ii*) the high-frequency C_p roll-off is due to the access impedance and the intrinsic C_p profile is, as expected, frequency-independent [42]; *iii*) the peak in the intrinsic G_p/ω profile, usually related to defects response [43], was hidden by the access impedance. The real one is much lower than that observed in Fig. 4 and occurs at lower frequencies.

To validate the extracted Z_{SER} value we performed independent physics-based C-f/G-f simulations of a 10nm MFM stack (reported in Fig. 6a), for simplicity only at 0V. Such physics-based simulations are carried out using Ginestra® simulation platform [37], which includes Schottky and thermionic emission, direct (WKB approximation), trap-

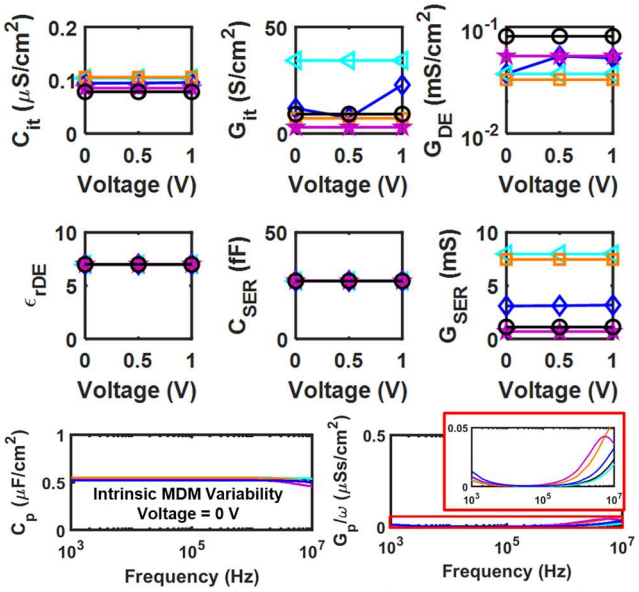

Fig. 8 – Extracted MDM model parameters and intrinsic response of devices in Fig. 6, obtained by removing the series impedance component from the MDM model.

assisted tunneling (TAT – including trap-to-trap contribution), and Fowler-Nordheim tunneling, as well as the trapped charge term in the Poisson's equation. We include defects in the HfO_2 bulk (defects density $\delta = 10^{20} cm^{-3}$ with a normal distribution in space centered at the middle of the stack and a uniform lateral distribution) having thermal (E_{TH} = 2.1±1 eV) and relaxation (E_{REL} = 1.2 eV) energies [44] which are very close to those predicted by hybrid-DFT calculations for oxygen vacancies in the orthorhombic ferroelectric phase of HfO_2 ($E_{TH} \approx 1.8$ eV, $E_{REL} \approx 0.7$ eV) [45]. Consistently with the value extracted from experiments using the small-signal compact model we imposed an equivalent $\epsilon_{rFE}(0V) = 26$, in order to effectively include the presence of different HZO phases (e.g., orthorhombic, monoclinic, and tetragonal).

Results are reported in Fig. 6b and show that the measured C_p and G_p/ω profiles (blue symbols) can be only reproduced by including a parasitic series impedance equal to the extracted Z_{SER} (black lines), while simulations without the parasitic impedance (red dashed lines) show very similar profiles to those of the intrinsic MFM in Fig. 5, especially for the C_p profile, (Fig. 6b). The simulated G_p/ω profile presents high and low frequency behavior in quantitative agreement with those of the intrinsic device as retrieved by excluding the Z_{SER} contribution from experimental data using the compact model. However, the peak amplitude and position in the mid-frequency range are slightly different. This can be explained by the simplifications adopted in simulations, i.e., we included just one defect species (oxygen vacancies) and neglected the presence of possible interfacial layers and different HZO phases, which would be needed to carefully model the complex dynamics of a real stack [46]–[48]. However, in this work we are mainly interested in the analysis of qualitative trends rather than in the precise and comprehensive investigation of the underlying complex phenomena.

The same experiments are also repeated for different MDM stacks (Figs. 7-8), revealing the intrinsic behavior of these capacitors, which show a defects response in the G_p/ω profile at much higher frequencies compared to the MFM. Differently form Fig. 3, which reports results for MDM with t_{DE} = 6nm,

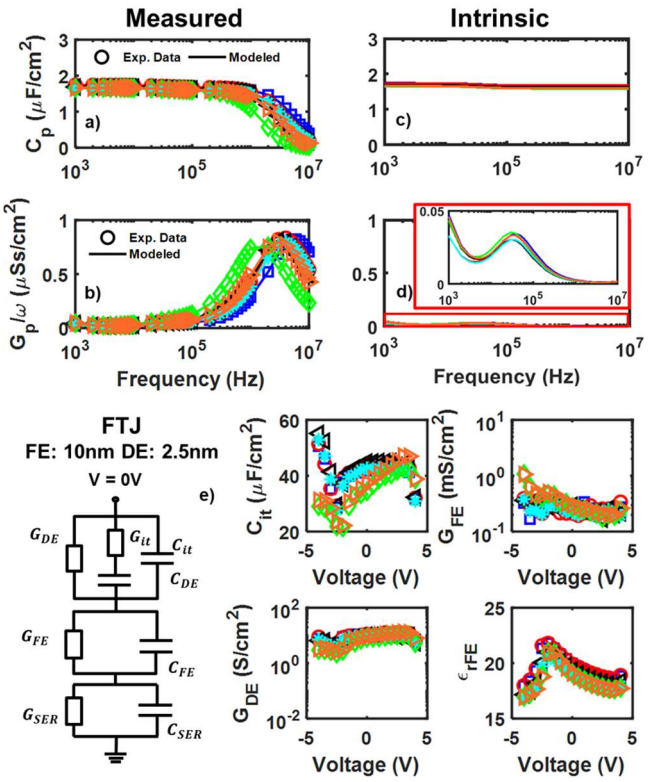

Fig. 9 – a-b) FTJ measured device-to-device variability, comparing FTJs with t_{DE} =2.5nm, with different areas and bottom tip positions (as in Figs. 4 and 7). c-d) Intrinsic FTJ frequency response, revealing the actual device to device variability. e) FTJ small signal model and extracted parameters of interest. C_{SER} and G_{SER} are not shown since they are not considered for the evaluation of the intrinsic profiles.

Fig. 7 shows also that 10nm MDMs present much lower (as expected) G_{DE}s in [0 +1] V. The trend is found to be almost constant within the applied voltage range, most probably because of the noise floor limitation of the measurement setup. A G_{DE} increase would then be visible at larger voltages, however respecting the trends in Fig. 3. As for thinner MDM, traps response is still weakly dependent on bias.

IV. Ferroelectric Tunnel Junctions

In Fig. 9a-b, the measurement results of an FTJ with a t_{DE} value of 2.5 nm at 0V are shown for devices with different areas and tip positions. By analyzing these results, it is possible to extract the intrinsic profiles, depicted in Fig. 9c-d, and parameters (shown in Fig. 9e) by plotting C_p and G_p/ω discounting the Z_{SER} parameters. As expected, the G_{FE} values, presented in Fig. 9e, are similar to those of the MFM (shown in Fig. 5), as both devices have a t_{FE} of 10 nm. It is worth noting that the frequencies and values of the G_p/ω peak in the FTJ devices are similar to those in the MFM devices, which suggests that the intrinsic response of the FTJ is more sensitive to defects in the FE rather than defects in the DE or at the FE/DE interface.

This comparison between the results obtained on FTJs and those obtained on MFM and MDM structures helps to better understand the response measured on FTJs.

V. Discussion

Repeating the experiments for FTJs with different t_{DE} it is possible to compare the extracted parameters and devices response with those of the MFM and MDM capacitors. As

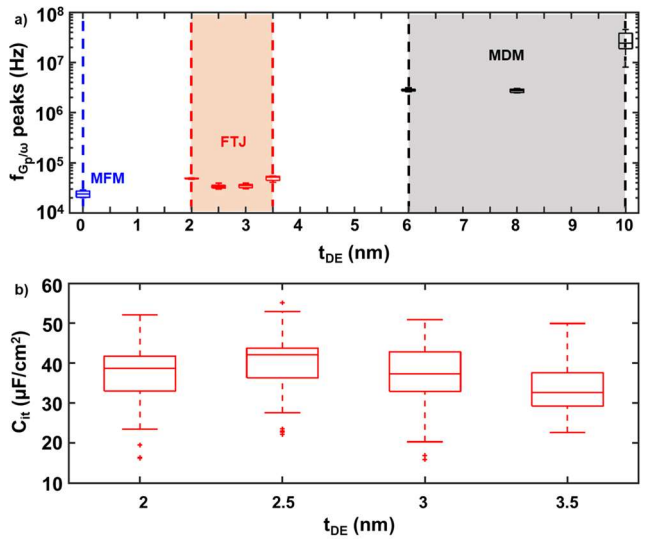

Fig. 10 – a) Comparison between the extracted G_p/ω peak's amplitudes for MFMs (blue), FTJs (red) and MDMs (black), revealing the similarity between FTJs and MFMs. b) Comparison of extracted C_{it} vs. t_{DE} in FTJs. For each t_{DE}, the reported C_{it} ranges consider the parameter voltage dependence and include device to device variability (as in Fig. 9). No trend is found.

mentioned before, FTJ G_p/ω peak's frequencies are much more similar to those of MFM capacitors (reported in Fig. 10a) rather than those of MDMs, several orders of magnitude above the others. This further confirms the role of FE properties and defects nature in determining the small-signal response for FTJ devices. Furthermore, the extracted C_{it} values for FTJs show no trend with t_{DE}, indicating a negligible relation between the DE-FE interface impurities and DE thickness.

Fig. 11a reports the G_{DE} vs. t_{DE} exponential trend obtained by interpolating the values extracted for different MDM capacitors, compared with those extracted from FTJs. The latter show higher than expected values with a very mild dependence on t_{DE}. This is also confirmed by ultra-low frequency IV measurements (execution time = 132s), Fig. 11b, which reveal that FTJs with $t_{DE} \leq 3$nm all have similar leakage. This confirms that the ultra-thin DE layer in FTJs is highly defective and dominated by impurities probably out-diffusing from the interfaces with the top TiN electrode and the FE. However, t_{DE} is found to modulate the FE properties, specifically the voltage dependence of ϵ_{rFE} and the G_p/ω peak. Fig. 12a shows that increasing t_{DE} results in lower and more compact ϵ_{rFE} profiles, suggesting that a thicker DE can partially inhibit the orthorhombic phase formation during the annealing process, affecting the switching. Arguably, this is a local phenomenon expected to occur close to the DE/FE interface. Furthermore, the effect of t_{DE} is also visible in the analysis of the G_p/ω peaks at 0V, as reported in Fig. 12b, suggesting an inverse relation between t_{DE} and ferroelectric domain response. Interestingly, the extracted ϵ_{rFE} and G_p/ω peak values show a linear correlation, Fig. 12c, reinforcing the idea that the G_p/ω peak is not only related to defects as usually thought [43], but is also related to the overall FE phase composition. Thus, extra care must be adopted when assessing the interface defects density based only on G_p/ω peaks [43] as this can easily lead to wrong conclusions. It is therefore arguable that the dielectric thickness may have an influence, specifically during the post-deposition annealing, on the formation and physical composition of the expectedly disordered parasitic layer between the FE and DE [39], [40],

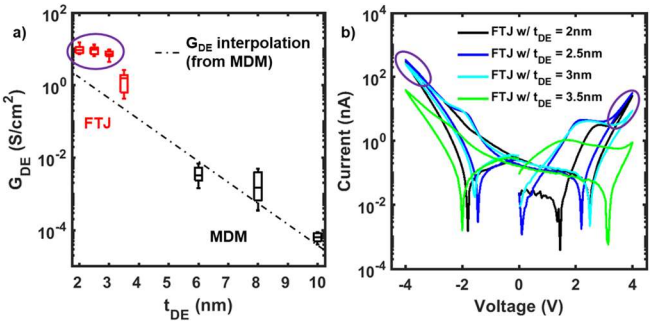

Fig. 11 – a) G_{DE} vs. t_{DE} in MDMs (black) and FTJs (red). FTJs present higher than expected G_{DE} values, highlighting the increase (and saturation (purple circle)) of DE defectivity with reducing its thickness. b) Slow IV measurements (execution time = 132s) with a reduced capacitive current (dV/dt) to highlight the leakage contribution emphasize the similarity for FTJs with $t_{DE} \leq 3$nm (purple circle), confirming the findings in (a).

[49]. Such a layer is expected to have a lower permittivity compared to that typical of ferroelectric HfO_2, which would result in an effective change in the observed ϵ_{rFE} parameter as extracted from our experiments. Along the same line, t_{DE} is found to influence also the intrinsic conductance of the FE layer, G_{FE}, especially at negative voltages, Fig. 13.

To confirm the found trend, the same MFM stack of Fig. 6a is simulated again in Ginestra® by changing the ϵ_{rFE} value in order to mimic the effect on the FE layer resulting from the insertion of a DE layer during the fabrication process. Simulation results show an almost linear relation between ϵ_{rFE} and G_p/ω peak's amplitude (Fig. 14), qualitatively in agreement with the trend extracted from measurements and model extractions from all FTJs, as shown in Fig. 12. Moreover, by changing the ϵ_{rFE} the low-frequency G_p/ω tail changes as well, which is associated to a larger leakage, in turn dominated by the intrinsic FE conductance [33], [34], which is in agreement with the experimental results in Fig. 12c, further stressing the role of FE properties on G_p/ω response [36].Then, the increase of the G_p/ω peak's values would be mostly related to the FE leakage increase because of the constant defect's contribution, which can indeed be mainly associated to the frequency of the G_p/ω peak.

VI. Conclusions

In this work, we introduced and validated an advanced FTJ small-signal compact model that accounts for separate leakage contributions in the FE and DE layers, the contribution of a parasitic series impedance, and non-uniform crystalline FE phase. The model correctly reproduces measurements taken on different devices in different conditions and with different tips position, allowing a more refined investigation on sample layout and material properties effects on the entire device under measurement. In particular, the possibility to isolate and remove the parasitic impedance between the actual device and the bottom tip, validated by physics-based simulation in Ginestra® simulation platform [37], allows the analysis of the desired intrinsic devices properties and variability.

Results are obtained by comparing the study of single layer MFM and MDM capacitors with MDFM FTJs. The insertion of t_{DE} in FTJs, although weakly effective in leakage control due to the found high defectivity, is revealed to be a possible cause for inhibiting the ferroelectric orthorhombic phase formation in HZO layer or, equivalently, for promoting the erosion of a portion of the FE layer resulting in the formation

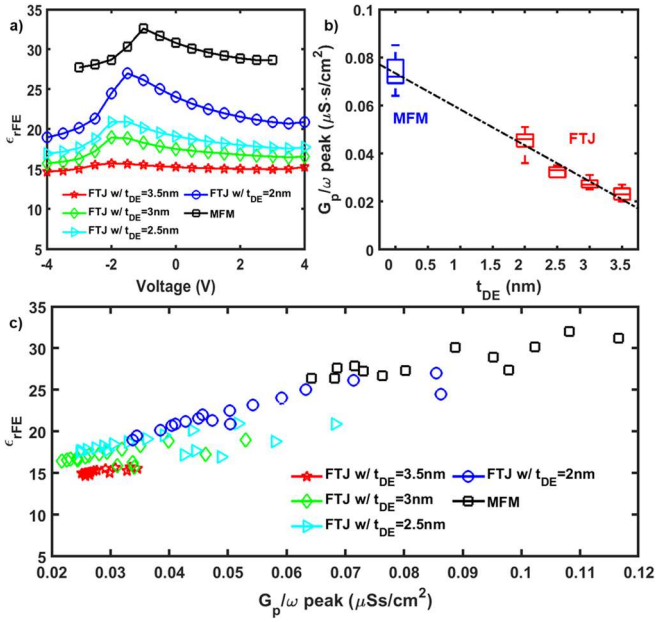

Fig. 12 – a) Extracted ϵ_{rFE} voltage dependence for MFM and FTJs with different t_{DE}. Thicker DE corresponds to lower and more compact profiles. This suggests a relation between larger t_{DE} and a stronger inhibition of the orthorhombic phase formation, confirmed also by b) in which the trend of G_p/ω peaks vs. t_{DE} is shown (only for measurements at 0V). c) ϵ_{rFE} vs. G_p/ω peaks for MFM and FTJs with different t_{DE} shows a linear trend. Results are shown for a single device per sample (different symbols and colours) and for all voltages.

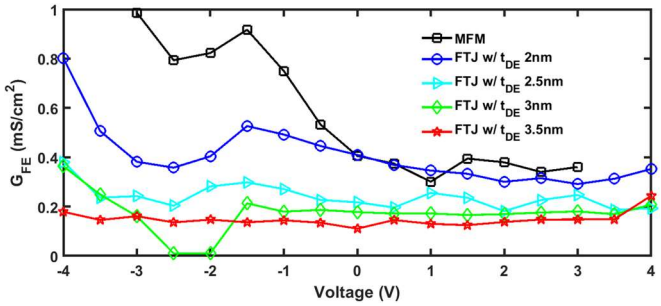

Fig. 13 – Comparison of the $G_{FE}(V)$ extracted by using the small-signal model for the MFM capacitor and FTJs. Larger G_{FE} is found for thinner DE layers, especially for negative voltages.

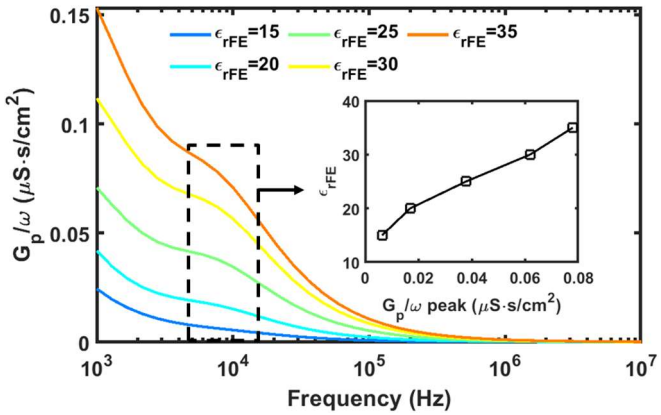

Fig. 14 – Simulated G_p/ω vs. frequency profiles for different ϵ_{rFE} values for the MFM stack of Fig. 6a. A linear trend is found between ϵ_{rFE} and G_p/ω peaks. A larger low-frequency tail is observed for higher ϵ_{rFE} which is associated with larger FE conductance.

of a parasitic non-ferroelectric layer with different dielectric properties. The equivalent fraction of orthorhombic phase, that is strictly related to ϵ_{rFE}, is also found to be approximately linearly related to the peak value of the G_p/ω vs. frequency curve, as also confirmed by physics-based simulations. The found relation between G_p/ω peak's amplitude and ϵ_{rFE} (the changes of which are suggested to be related to t_{DE}), would be also explained as a direct consequence of the direct proportionality between ϵ_{rFE} and G_{FE} (dictating the low-frequency behavior [33], [34]), suggesting that the typically adopted estimation methods for interface trap density may be misleading.

ACKNOWLEDGMENTS

The authors would like to express gratitude to NaMLab for providing the devices. They also acknowledge Applied Materials Italy for their support with Ginestra® device simulation software [37]. The work is funded by the H2020 BeFerroSynaptic (GA 871737) project. The content reflects the authors' results, but not necessarily the opinion of the EC.

REFERENCES

[1] D. Silver *et al.*, "Mastering the game of Go with deep neural networks and tree search," *Nature*, vol. 529, no. 7587, 2016, doi: 10.1038/nature16961.

[2] J. Gubbi, R. Buyya, S. Marusic, and M. Palaniswami, "Internet of Things (IoT): A vision, architectural elements, and future directions," *Future Generation Computer Systems*, vol. 29, no. 7, 2013, doi: 10.1016/j.future.2013.01.010.

[3] F. Arena and G. Pau, "An overview of big data analysis," *Bulletin of Electrical Engineering and Informatics*, vol. 9, no. 4, 2020, doi: 10.11591/eei.v9i4.2359.

[4] G. Kumar and S. Agrawal, "CMOS limitations and futuristic carbon allotropes," in *2017 8th IEEE Annual Information Technology, Electronics and Mobile Communication Conference, IEMCON 2017*, 2017. doi: 10.1109/IEMCON.2017.8117151.

[5] M. Horowitz, "1.1 Computing's energy problem (and what we can do about it)," in *Digest of Technical Papers - IEEE International Solid-State Circuits Conference*, 2014, vol. 57. doi: 10.1109/ISSCC.2014.6757323.

[6] M. T. Bohr and I. A. Young, "CMOS Scaling Trends and beyond," *IEEE Micro*, vol. 37, no. 6, 2017, doi: 10.1109/MM.2017.4241347.

[7] J. Backus, "Can Programming Be Liberated from the von Neumann Style? A Functional Style and Its Algebra of Programs," *Commun ACM*, vol. 21, no. 8, 1978, doi: 10.1145/359576.359579.

[8] Wm. A. Wulf and S. A. McKee, "Hitting the memory wall," *ACM SIGARCH Computer Architecture News*, vol. 23, no. 1, 1995, doi: 10.1145/216585.216588.

[9] E. Strubell, A. Ganesh, and A. McCallum, "Energy and policy considerations for deep learning in NLP," in *ACL 2019 - 57th Annual Meeting of the Association for Computational Linguistics, Proceedings of the Conference*, 2020.

[10] G. Indiveri and S. C. Liu, "Memory and Information Processing in Neuromorphic Systems," *Proceedings of the IEEE*, vol. 103, no. 8. 2015. doi: 10.1109/JPROC.2015.2444094.

[11] T. Zanotti, F. M. Puglisi, and P. Pavan, "Smart Logic-in-Memory Architecture for Low-Power Non-Von Neumann Computing," *IEEE Journal of the Electron Devices Society*, vol. 8, 2020, doi: 10.1109/JEDS.2020.2987402.

[12] W. Wan *et al.*, "A compute-in-memory chip based on resistive random-access memory," *504 | Nature |*, vol. 608, 2022, doi: 10.1038/s41586-022-04992-8.

[13] M. le Gallo and A. Sebastian, "An overview of phase-change memory device physics," *Journal of Physics D: Applied Physics*, vol. 53, no. 21. 2020. doi: 10.1088/1361-6463/ab7794.

[14] F. Zahoor, T. Z. Azni Zulkifli, and F. A. Khanday, "Resistive Random Access Memory (RRAM): an Overview of Materials, Switching Mechanism, Performance, Multilevel Cell (mlc) Storage, Modeling, and Applications," *Nanoscale Research Letters*, vol. 15, no. 1. 2020. doi: 10.1186/s11671-020-03299-9.

[15] M. Lanza *et al.*, "Memristive technologies for data storage, computation, encryption, and radio-frequency communication," *Science*, vol. 376, no. 6597. American Association for the

Advancement of Science, Jun. 03, 2022. doi: 10.1126/science.abj9979.

[16] S. Kvatinsky, G. Satat, N. Wald, E. G. Friedman, A. Kolodny, and U. C. Weiser, "Memristor-based material implication (IMPLY) logic: Design principles and methodologies," *IEEE Trans Very Large Scale Integr VLSI Syst*, vol. 22, no. 10, 2014, doi: 10.1109/TVLSI.2013.2282132.

[17] E. Lehtonen and M. Laiho, "Stateful implication logic with memristors," in *2009 IEEE/ACM International Symposium on Nanoscale Architectures, NANOARCH 2009*, 2009. doi: 10.1109/NANOARCH.2009.5226356.

[18] T. Zanotti, P. Pavan, and F. M. Puglisi, "Multi-Input Logic-in-Memory for Ultra-Low Power Non-Von Neumann Computing," *Micromachines*, 2021, doi: 10.3390/mi12101243.

[19] G. Indiveri *et al.*, "Neuromorphic silicon neuron circuits," *Frontiers in Neuroscience*, no. May, 2011. doi: 10.3389/fnins.2011.00073.

[20] D. Gandolfi *et al.*, "Emergence of associative learning in a neuromorphic inference network," *J Neural Eng*, 2022, doi: 10.1088/1741-2552/ac6ca7.

[21] D. V. Christensen *et al.*, "2022 roadmap on neuromorphic computing and engineering," *Neuromorphic Computing and Engineering*, vol. 2, no. 2, 2022, doi: 10.1088/2634-4386/ac4a83.

[22] R. Materlik, C. Kunneth, and A. Kersch, "The origin of ferroelectricity in Hf1-xZrxO2: A computational investigation and a surface energy model," *J Appl Phys*, vol. 117, no. 13, 2015, doi: 10.1063/1.4916707.

[23] S. J. Kim, J. Mohan, S. R. Summerfelt, and J. Kim, "Ferroelectric Hf0.5Zr0.5O2 Thin Films: A Review of Recent Advances," *JOM*, vol. 71, no. 1. 2019. doi: 10.1007/s11837-018-3140-5.

[24] R. Yang, "In-memory computing with ferroelectrics," *Nature Electronics*, vol. 3, no. 5. 2020. doi: 10.1038/s41928-020-0411-2.

[25] S. Oh, H. Hwang, and I. K. Yoo, "Ferroelectric materials for neuromorphic computing," *APL Mater*, vol. 7, no. 9, 2019, doi: 10.1063/1.5108562.

[26] L. Bégon-Lours *et al.*, "Scaled, Ferroelectric Memristive Synapse for Back-End-of-Line Integration with Neuromorphic Hardware," *Adv Electron Mater*, vol. 8, no. 6, 2022, doi: 10.1002/aelm.202101395.

[27] T. Ali *et al.*, "Impact of the Ferroelectric and Interface Layer Optimization in an MFIS HZO based Ferroelectric Tunnel Junction for Neuromorphic based Synaptic Storage," in *2021 Silicon Nanoelectronics Workshop, SNW 2021*, 2021. doi: 10.1109/SNW51795.2021.00032.

[28] B. Max, M. Hoffmann, S. Slesazeck, and T. Mikolajick, "Direct Correlation of Ferroelectric Properties and Memory Characteristics in Ferroelectric Tunnel Junctions," *IEEE Journal of the Electron Devices Society*, vol. 7, 2019, doi: 10.1109/JEDS.2019.2932138.

[29] B. Max, T. Mikolajick, M. Hoffmann, and S. Slesazeck, "Retention characteristics of Hf0.5Zr0.5O2-based ferroelectric tunnel junctions," in *2019 IEEE 11th International Memory Workshop, IMW 2019*, 2019. doi: 10.1109/IMW.2019.8739765.

[30] M. Dragoman, M. Aldrigo, D. Dragoman, S. Iordanescu, A. Dinescu, and M. Modreanu, "HfO2-Based Ferroelectrics Applications in Nanoelectronics," *Physica Status Solidi - Rapid Research Letters*, vol. 15, no. 5, 2021, doi: 10.1002/pssr.202000521.

[31] K. Y. Hsiang *et al.*, "Ferroelectric HfZrO2with Electrode Engineering and Stimulation Schemes as Symmetric Analog Synaptic Weight Element for Deep Neural Network Training," *IEEE Trans Electron Devices*, vol. 67, no. 10, 2020, doi: 10.1109/TED.2020.3017463.

[32] A. R. West, D. C. Sinclair, and N. Hirose, "Characterization of Electrical Materials, Especially Ferroelectrics, by Impedance Spectroscopy," Kluwer Academic Publishers, 1997.

[33] L. Benatti and F. M. Puglisi, "Understanding the Reliability of Ferroelectric Tunnel Junction Operations using an Advanced Small-Signal Model," in *IEEE International Integrated Reliability Workshop Final Report*, 2021, vol. 2021-October. doi: 10.1109/IIRW53245.2021.9635621.

[34] L. Benatti and F. M. Puglisi, "Impedance Investigation of MIFM Ferroelectric Tunnel Junction using a Comprehensive Small-Signal Model," *IEEE Transactions on Device and Materials Reliability*, 2022, doi: 10.1109/TDMR.2022.3182941.

[35] L. Benatti, S. Vecchi, and F. M. Puglisi, "Impedance Spectroscopy of Ferroelectric Capacitors and Ferroelectric Tunnel Junctions," in *Presented at IEEE International Integrated Reliability Workshop Final Report*, 2022.

[36] L. Benatti, P. Pavan, and F. M. Puglisi, "Combining Experiments and a Novel Small Signal Model to Investigate the Degradation Mechanisms in Ferroelectric Tunnel Junctions," in *IEEE International Reliability Physics Symposium Proceedings*, 2022, vol. 2022-March, pp. P61–P65. doi: 10.1109/IRPS48227.2022.9764602.

[37] "https://www.appliedmaterials.com/products/applied-mdlx-ginestrasimulation-software."

[38] S. J. Kim *et al.*, "Ferroelectric TiN/Hf0.5Zr0.5O2/TiN Capacitors with Low-Voltage Operation and High Reliability for Next-Generation FRAM Applications," in *2018 IEEE 10th International Memory Workshop, IMW 2018*, 2018. doi: 10.1109/IMW.2018.8388832.

[39] K. Ni *et al.*, "Critical Role of Interlayer in Hf0.5Zr0.5O2 Ferroelectric FET Nonvolatile Memory Performance," *IEEE Trans Electron Devices*, vol. 65, no. 6, 2018, doi: 10.1109/TED.2018.2829122.

[40] K. Toprasertpong, M. Takenaka, and S. Takagi, "Direct Observation of Interface Charge Behaviors in FeFET by Quasi-Static Split C-V and Hall Techniques: Revealing FeFET Operation," in *Technical Digest - International Electron Devices Meeting, IEDM*, 2019, vol. 2019-December. doi: 10.1109/IEDM19573.2019.8993664.

[41] M. Y. Kao *et al.*, "Variation Caused by Spatial Distribution of Dielectric and Ferroelectric Grains in a Negative Capacitance Field-Effect Transistor," *IEEE Trans Electron Devices*, vol. 65, no. 10, 2018, doi: 10.1109/TED.2018.2864971.

[42] B. Lin, G. Choe, J. Hur, A. I. Khan, S. Yu, and H. Wang, "Experimental RF Characterization of Ferroelectric Hafnium Zirconium Oxide Material at GHz for Microwave Applications," in *Device Research Conference - Conference Digest, DRC*, 2021, vol. 2021-June. doi: 10.1109/DRC52342.2021.9467202.

[43] Y. Qu, J. Li, M. Si, X. Lyu, and P. D. Ye, "Quantitative Characterization of Interface Traps in Ferroelectric/Dielectric Stack Using Conductance Method," *IEEE Trans Electron Devices*, vol. 67, no. 12, 2020, doi: 10.1109/TED.2020.3034564.

[44] L. Benatti, S. Vecchi, M. Pesic, and F. M. Puglisi, "The Role of Defects and Interface Degradation on Ferroelectric HZO Capacitors Aging," in *Accepted at IEEE International Reliability Physics Symposium Proceedings*, 2023.

[45] M. Pesic *et al.*, "Variability sources and reliability of 3D-FeFETs," in *IEEE International Reliability Physics Symposium Proceedings*, 2021, vol. 2021-March. doi: 10.1109/IRPS46558.2021.9405118.

[46] M. Pešić *et al.*, "Physical Mechanisms behind the Field-Cycling Behavior of HfO2-Based Ferroelectric Capacitors," *Adv Funct Mater*, vol. 26, no. 25, pp. 4601–4612, Jul. 2016, doi: 10.1002/adfm.201600590.

[47] Y. Cheng *et al.*, "Reversible transition between the polar and antipolar phases and its implications for wake-up and fatigue in HfO2-based ferroelectric thin film," *Nat Commun*, vol. 13, no. 1, 2022, doi: 10.1038/s41467-022-28236-5.

[48] F. P. G. Fengler, M. Hoffmann, S. Slesazeck, T. Mikolajick, and U. Schroeder, "On the relationship between field cycling and imprint in ferroelectric Hf0.5Zr0.5O2," *J Appl Phys*, vol. 123, no. 20, 2018, doi: 10.1063/1.5026424.

[49] S. Lancaster *et al.*, "Investigating charge trapping in ferroelectric thin films through transient measurements," *Frontiers in Nanotechnology*, vol. 4, Aug. 2022, doi: 10.3389/fnano.2022.939822.